

1 **A new analytical method for stability analysis of rock blocks with** 2 **cavities in sub-horizontal strata by the considering eccentricity effect**

3 Xushan Shi¹, Bo Chai^{1,3,4}, Juan Du^{1,2,4}, Wei Wang^{1,3,4}, Bo Liu¹

4 ¹School of Environmental Studies, China University of Geosciences, Wuhan, 430078, China

5 ²Centre for severe weather and climate and hydrogeological hazards, Wuhan, 430078, China

6 ³Hubei Key Laboratory of Yangtze Catchment Environmental Aquatic Science, Wuhan, 430078, China

7 ⁴Research Center for Geohazards Monitoring and Warning in Three Gorges Reservoir, Wanzhou, 404000, China

8 *Correspondence to:* Bo Chai (chaibo@cug.edu.cn) and Juan Du (dujuan@cug.edu.cn)

9 **Abstract.** The basal cavity of a rock block formed due to differential weathering is an important predisposing factor for rockfall
10 in hard-soft interbedded rocks, which induces eccentricity effect at the base of the rock block. Rock block falling due to the
11 eccentricity effect with the failure modes of toppling or sliding is defined as biased rockfall in this study. Taking into account
12 the non-uniform stress distribution due to the eccentricity effect, a new analytical method is proposed for three-dimensional
13 stability force and stability of biased rockfall. The development of non-uniform stress distribution stress calculated by this
14 analytical method was verified by numerical simulation. The biased rockfall progresses from partial damage of the soft
15 underlying layer, caused by non-uniform distributed stress, to toppling and sliding of overhanging hard rock block due to
16 overall unbalanced force. Therefore, a set of factors of safety (*Fos*) against partial damage (compressive and tensile damage
17 of the soft underlying layer) and overall failure (toppling and sliding of the hard rock block) are used to determine the rockfall
18 susceptibility level. The analytical method is applied and validated using biased rockfalls on the northeast edge of the Sichuan
19 Basin in Southwest China, where a significant number of rockfalls consisting of overhanging thick sandstone and underlying
20 mudstone occur. The evolution process of biased rockfalls is divided into four stages, initial state, cavity formation,
21 partial unstable and failure. The proposed method is validated by calculating *Fos* of the typical unstable rock blocks in the
22 study area. As the cavity continues to grow, the continuous retreat of cavity causes stress redistribution between the hard and
23 soft rock layers. This results in damage to the underlying soft rock layer due to the development of the eccentricity effect,
24 ultimately leading to the failure of the hard rock block. The critical cavity retreat ratio is determined to be 0.33, which is used
25 to classify the low and moderate rockfall susceptibility in the eastern Sichuan Basin. The proposed analytical method provides
26 insights into the evolution of biased rockfall and a means for early identification and susceptibility assessment of rockfall.

27 **List of symbols**

28 *a* length of the block along the *x* direction

29 *A* area of contact surfaces

30 *b* width of the block along the *y* direction

31 *c* cohesive force of the mudstone

32	d_i	width of the basal cavity in a certain direction
33	e_x	eccentric distance along the x direction
34	e_y	eccentric distance along the y direction
35	E_x	horizontal seismic force along the x direction
36	Fos	factor of safety
37	h	height of the block
38	h_w	height of the water in the fracture
39	H_x	water pressure along the x direction
40	I_x	moment of inertia with respect to the x -axis
41	I_y	moment of inertia with respect to the y -axis
42	k_e	earthquake contribution coefficient
43	k_1	rainfall coefficient, taking 1 in the rainfall scenario and 0 in the non-rainfall scenario
44	k_2	earthquake coefficient, taking 1 in the seismic scenario and 0 in the non-seismic scenario
45	k_3	free surface coefficient, taking 1 for two free surfaces and 0 for three free surfaces
46	M_{bx}	total bending moments with respect to the x -axis on the mudstone foundation
47	M_{by}	total bending moments with respect to the y -axis on the mudstone foundation
48	M_{bEx}	bending moment of E_x with respect to the x -axis on the mudstone foundation
49	M_{bHx}	bending moment of H_x with respect to the x -axis on the mudstone foundation
50	M_{bWx}	bending moment of W with respect to the x -axis on the mudstone foundation
51	M_{Ex}	overturning moment provided by E_x along the x direction
52	M_{Hx}	overturning moment provided by H_x along the x direction
53	M_{px}	stabilizing moment of p_n along the x direction
54	$M_{W_{inx}}$	stabilizing moment provided by W along the x direction
55	$M_{W_{outx}}$	overturning moment provided by W along the x direction
56	N_z	total applied vertical load on the mudstone base
57	O	origin of the (x, y) coordinates
58	$p(x, y)$	pressure magnitude at point (x, y)
59	r_i	the basal cavity retreat ratio equal to the ratio of cavity width to block width in a certain direction
60	W	weight of the block
61	x	distance to O along the x -axis
62	y	distance to O along the y -axis
63	α	true dip of the contact surface
64	γ_s	unit weight of sandstone

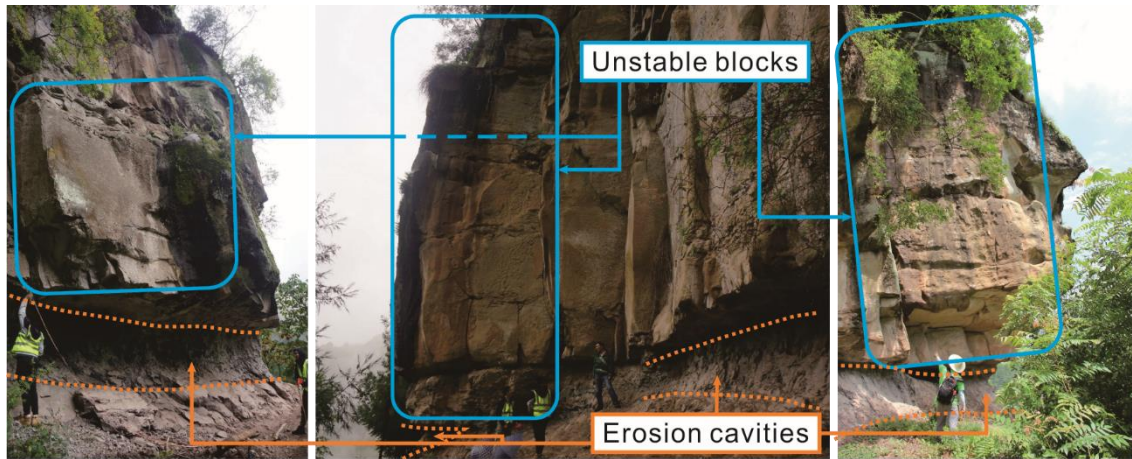
65	γ_w	unit weight of water
66	θ_1	apparent dip of α on plane J1
67	θ_2	apparent dip of α on plane J2
68	σ_{cmax}	ultimate compressive strength of the mudstone
69	σ_{tmax}	ultimate tensile strength of the mudstone
70	τ_{max}	ultimate shear strength of the mudstone
71	φ	friction angle of the mudstone
72	ω_1	angle between the trend of the contact surface and the x direction
73	ω_2	angle between the trend of the contact surface and the y direction

74 **1 Introduction**

75 Rockfall is defined as the detachment of a rock block from a steep slope along a surface, on which little or no shear
76 displacement takes place ([Cruden and Varnes, 1996](#)). Rockfalls frequently occur in mountainous ranges, cut slopes, and coastal
77 cliffs, and they may cause significant facility damage and casualties in residential areas and transport corridors ([Chau et al.,](#)
78 [2003](#); [Volkwein et al., 2011](#); [Corominas et al., 2018](#)). Stability analysis of rock blocks are crucial for risk management and
79 early warning of rockfall ([Kromer et al., 2017](#)).

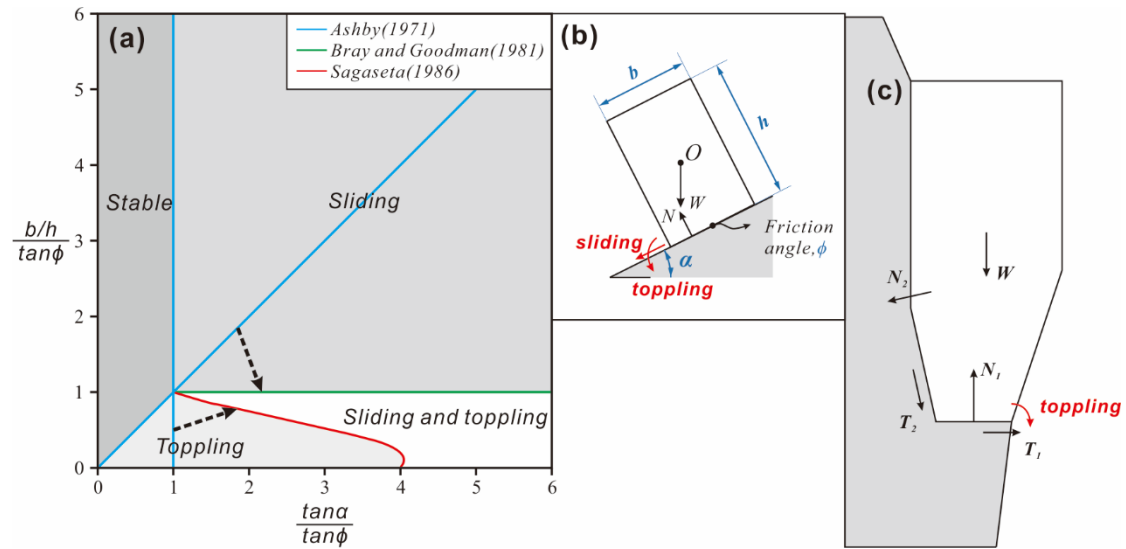
80 Rockfalls are prone to occur in soft-hard rock formations, and the non-uniform stress distribution caused by differential
81 weathering of rock formations is the main reason for the failure of rockfall. In the eastern Sichuan Basin, Southwest China,
82 rockfall is widespread and poses high risk ([Chen et al., 2008](#); [Chen and Tang, 2010](#); [Zhang et al., 2016](#); [Zhou et al., 2017](#);
83 [Zhou et al., 2018](#)). The rockfall in this area is attributed to the tectonic setting of Jura-type folds and the stratum sequence,
84 which is characterized by the interbedding of hard and soft layers. An alternation of thick sandstone and thin mudstone layers
85 is formed in the wide and gentle-angle synclines ([Zhang et al., 2015](#); [Wu et al., 2018](#)). Weathering is known to be one of the
86 main predisposing factors for rockfall ([Jaboyedoff et al., 2021](#); [Zhan et al., 2022](#)). The cliff comprised of hard sandstone is the
87 source of rockfall, and the underlying mudstone is more susceptible to weathering. Along with the retreat of basal cavities in
88 the mudstone layer, the gravity centre of the overhanging sandstone block moves outward relative to the mudstone. In this
89 case, the stress distribution in the contact surface of sandstone and mudstone is non-uniform. The mudstone on the outer side
90 bears higher compressive stress than that on the inner side. This phenomenon can be defined as an eccentricity effect, which
91 leads to mudstone damage and failure of the overhanging sandstone by toppling or sliding. This type of rockfall is defined as
92 biased rockfall in this study (Fig. 1). Similar rockfall patterns have been widely reported in other regions, such as Joss Bay in
93 England ([Hutchinson, 1972](#)), Okinawa Island in Japan ([Kogure et al., 2006](#)), and the Colorado Plateau of the southwestern
94 United States ([Ward et al., 2011](#)). Retreat of the basal cavity is a main cause for the failure of the overhanging block. Therefore,
95 it is necessary to establish an analytical method, considering the development of the basal cavity, to analyse the stress

96 distribution and stability of rock blocks, which is fundamental to the susceptibility assessment and risk control of biased
97 rockfall.



98 **Figure 1** Potential unstable blocks and basal cavities caused by differential weathering.

99
100 Rockfall stability analysis methods include statistical analysis ([Frattini et al., 2008](#); [Santi et al., 2009](#)), empirical rating systems
101 ([Pierson et al., 1990](#); [Ferrari et al., 2016](#)), and mechanical analysis ([Jaboyedoff et al., 2004](#); [Derron et al., 2005](#); [Matasci et al.,](#)
102 [2018](#)). The statistical analysis and empirical rating systems are suitable for rockfall hazard assessment at a regional scale. The
103 accuracy of statistical analysis depends on the completeness of rockfall inventories ([Chau et al., 2003](#); [Guzzetti et al., 2003](#);
104 [D'amato et al., 2016](#)). However, its application to rockfall hazards is limited due to the lack of complete inventory data ([Budetta](#)
105 [and Nappi, 2013](#); [Malamud et al., 2004](#)). Empirical and semi-empirical rating systems are used where site-specific rockfall
106 inventories are either unavailable or unreliable. Therefore, rockfall susceptibility can be assessed by heuristic ranking of
107 selected predisposing factors ([Frattini et al., 2008](#); [Budetta, 2004](#)). Mechanical analysis based on static equilibrium theory is
108 the main method to analyse the stability of site-specific rockfall using the factor of safety (Fos). [Ashby \(1971\)](#) conducted
109 stability analysis with a parallelepiped block resting on an inclined plane (Fig. 2a), and the solution was subsequently modified
110 by [Bray and Goodman \(1981\)](#) and [Sagaseta \(1986\)](#). [Kogure et al. \(2006\)](#) utilized a cantilever beam model to determine the
111 critical state of limestone cliffs. [Frayssines and Hantz \(2009\)](#) proposed the limit equilibrium method (LEM) to predict block
112 stability against sliding and toppling in steep limestone cliffs (Fig. 2c). [Chen and Tang \(2010\)](#) established a stability analysis
113 method of three types of unstable rocks in the Three Gorges Reservoir area with the LEM. [Alejano et al. \(2015\)](#) studied the
114 influence of rounding of block corners on the block stability. [Zhang et al. \(2016\)](#) defined Fos based on fracture mechanics and
115 studied the progressive failure process by analysing crack propagation. [Alejano et al. \(2010\)](#) and [Pérez-Rey et al. \(2021\)](#)
116 deduced a formula for Fos of blocks with more complex geometry.



117

118 **Figure 2** Traditional force analysis diagrams of the rock block. (a) and (b) are stability analysis diagrams of rock blocks under dynamic
 119 conditions, resting on an inclined plane with a dip angle of α . The rock block is generalized as a cuboid with dimensions $b \times h$ and weight
 120 W (as modified from [Ashby \(1971\)](#), [Bray and Goodman \(1981\)](#) and [Sagasetta \(1986\)](#)). (c) Force description of the toppling model proposed
 121 by [Frayssines and Hantz \(2009\)](#). In the above assumptions, N , T , and W are regarded as forces applied at a point.

122 The supporting force on the contact surface is assumed to be applied at a point in the current LEM methods (i.e., N in Fig. 2 b
 123 and c). However, the supporting force is actually a distributed force. The cavity generates an eccentricity effect on the
 124 overhanging rock block and results in a non-uniform distribution of the supporting force on the contact surface, which is not
 125 considered in the traditional LEM. The presence of non-uniform stress distribution plays a critical role in inducing localized
 126 damage within a rock mass. Damage is frequently considered as an indicator or a threshold for the onset of accelerated failure
 127 in rock masses (Zhang et al., 2016). Therefore, it is imperative to consider the non-uniform stress distribution for the rockfall
 128 stability analysis. Furthermore, most studies simplified the three-dimensional geometry of the rock block by one cross-section,
 129 which is used to represent the critical features of the slope structure. Nevertheless, for natural blocks with basal cavities, the
 130 cavities usually present different depths along different directions ([Pérez-Rey et al., 2021](#)). Therefore, a three-dimensional
 131 model is necessary to calculate the accurate stability. In addition, when a block has multiple free faces and a complex structure,
 132 its potential failure is dominated by different modes, including rock mass damage and overall block failure. Therefore, the
 133 probable failure modes should be determined prior to the calculation of FoS .

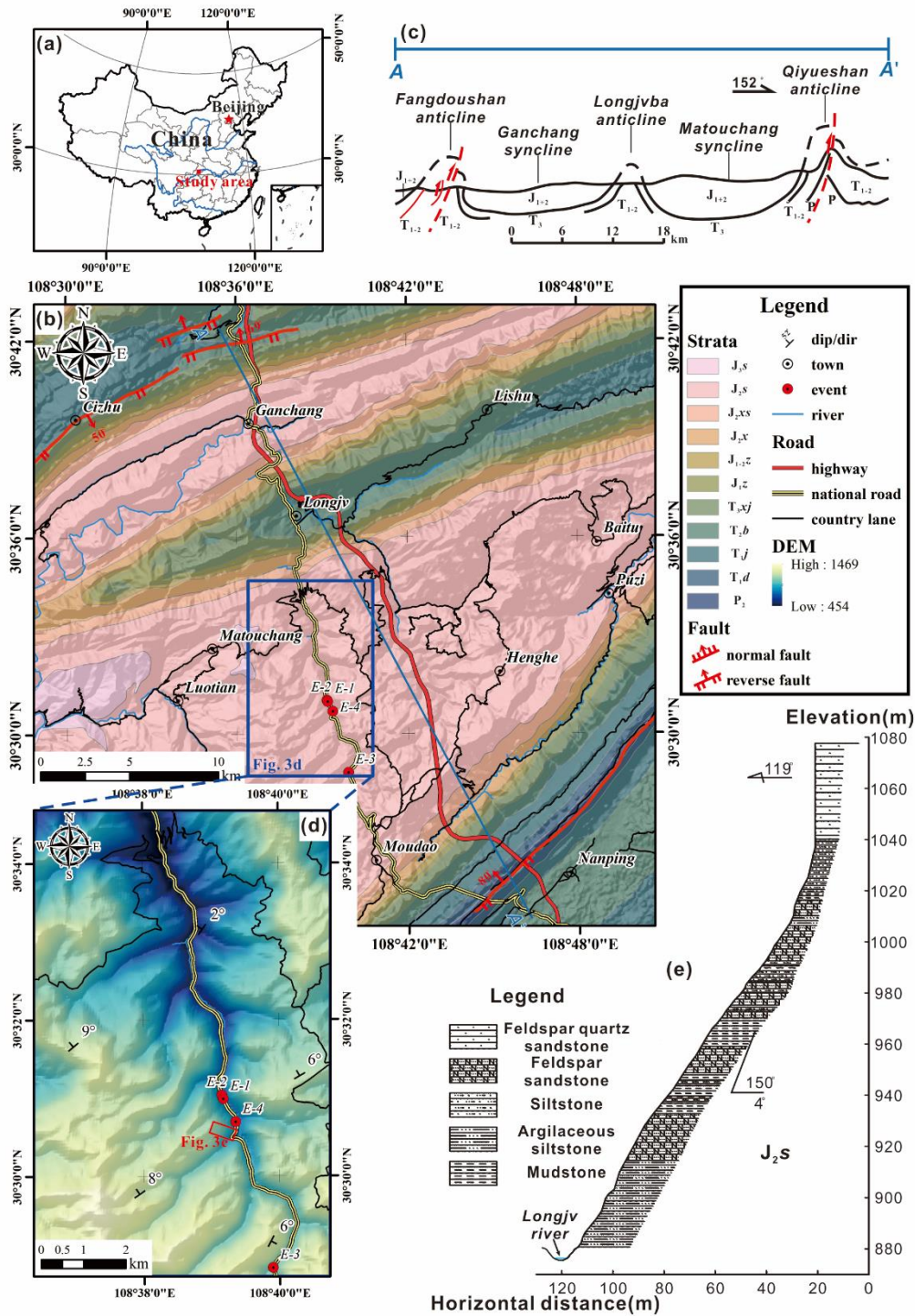
134 Based on rockfall investigation in the Eastern Sichuan Basin, China, the main objective of this study was to propose a new
 135 three-dimensional method for the determination of failure modes and FoS of biased rockfall, considering the non-uniform
 136 force distribution on the contact surfaces. Compared with the traditional LEM method, this study takes into account the partial
 137 damage of the underlying soft rock and the overall instability of the overhanging hard rock blocks, and can evaluate the stability
 138 of biased rockfall more comprehensively. FoS of the typical unstable rock blocks in the study area are calculated to validate
 139 the proposed method. In addition, the critical cavity retreat ratio in this area is analysed. This study is an extension of the basic

140 LEM for rockfall, which can promote the accuracy of rockfall stability analysis and facilitate rockfall prevention and risk
141 mitigation.

142 **2 Study area**

143 **2.1 Geological setting**

144 The study area is located on the northeastern edge of the Sichuan Basin, China (Fig. 3a). Continuous erosion processes generate
145 moderate-low mountain and valley landforms ([Yu et al., 2021](#)). The tectonic structure of this area is characterized by a series
146 of ENE anticlines and synclines (Fig. 3b, c). In the anticline area, the rock layers dip relatively steeply, where translational
147 rockslides are the main mode of slope failure. The syncline area is dominated by gently dipping strata and is prone to rockfall
148 ([Zhou et al., 2018](#)). The study area is located in the core of the Matouchang syncline, where the rock layers are sub-horizontal
149 (Fig. 3d, e). In this valley, due to the longstanding fluvial incision, the relative relief is approximately 500 m and the valley
150 flanks are extremely steep (Fig. 3e). In addition, the toes of the hill slopes are reshaped because of the construction of the
151 G318 national road, which is the main traffic line and is always threatened by rockfalls dropping from steep rock slopes (shown
152 in Fig. 3d and Table 1).



153

154 **Figure 3** (a) Location of the study area in China; (b) geological map of the study area; (c) tectonic sketch profile of A-A', whose location is
 155 showed in Fig. 3b; (d) rockfall-prone segment and key investigation areas. The red dots are the positions of historical rockfall events,

156 corresponding to the numbers in Table 1; (e) Geological cross-section of the hillslope in the Jitougou section of G318 national road, which
157 is marked by a red rectangle in Fig. 3d.

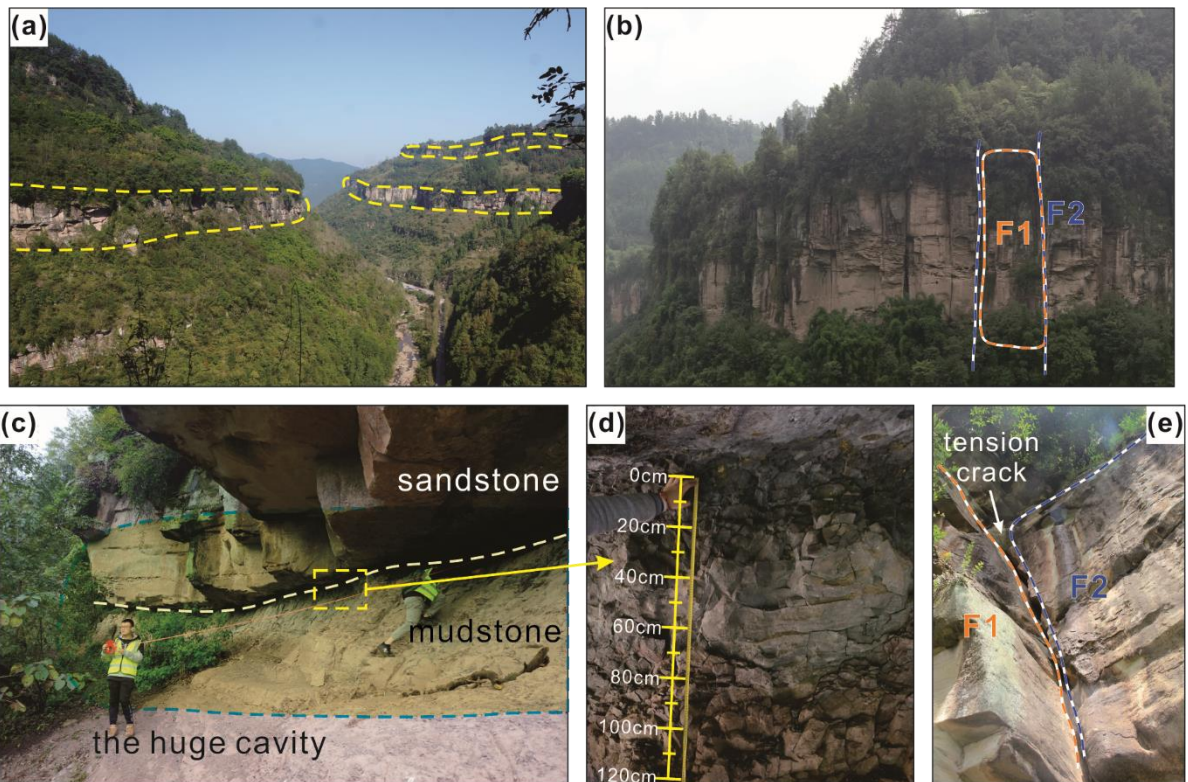
158 **Table 1** Historical rockfall events along G318 national road in the study area

No	Location	Time of occurrence (GMT+8)	Volume [m ³]	Consequence
E-1	K1698+900	2014-05 to 06*	Unknown	The power transmission facilities outside the road were smashed.
E-2	K1699+000	2015-02-14 23:00	About 240	A passing truck was stuck and two people dead.
E-3	K1690+700	2015-06-16	Unknown	The road was interrupted for a day.
E-4	K1698+400	2015-06-18 09:00	About 200	A vehicle was crashed into a gully and four people dead.

159 *Note: The exact time is unknown.

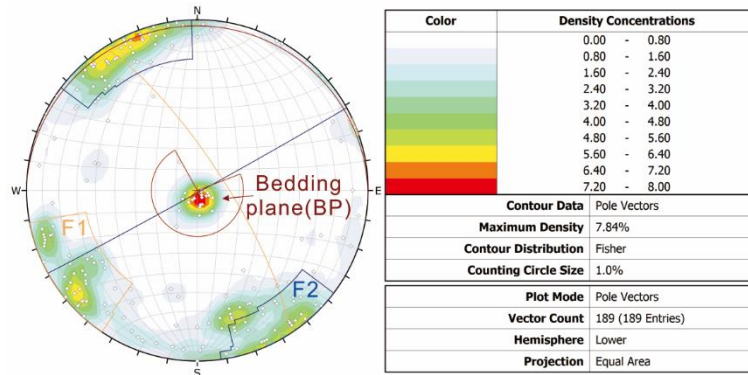
160 2.2 Rockfall characteristics

161 The slopes in the study area consist of a sub-horizontally interbedded sandstone and mudstone layer. Therefore, there are
162 multiple layers of potentially unstable rock blocks in the hill slopes (Fig 4a). The thick sandstone has two sets of sub-vertical
163 joints (Fig. 5), which cut the rock mass into blocks as the potential rockfall source (Fig. 4b). Cavities have formed in the
164 underlying mudstone layer (Fig. 4c, d). Joints and bedding planes (BP) constitute the detachment surfaces between the blocks
165 and steep slope (Fig. 4e). The eccentricity effect produced by the mudstone cavity plays an important role in the evolution
166 process of rockfall. When the basal mudstone cannot provide adequate supporting force, the blocks detach from the steep slope,
167 and biased rockfall occurs. Sliding and toppling are two possible failure modes of biased rockfall.



168

169 **Figure 4** Characteristics of biased rockfalls in the study area. (a) Multiple-layers of rockfall sources, which is consist of thick sandstone. (b)
 170 Two sets of sub-vertical joints (F1 and F2) recognized by the UAV photos. (c) Large basal cavity developed in the underlying mudstone. (d)
 171 Dense fractures on the mudstone surface generated by weathering and compression. (e) Vertical tension crack in the rear of the block, through
 172 which precipitation can infiltrate.
 173 According to the historical rockfall events in this area, precipitation is considered a triggering effect of rock instability. The
 174 precipitation mainly infiltrates along the sub-vertical joints or cracks of the sandstone (Fig. 4e). However, the drainage of
 175 fissure water is hysteretic due to the obstruction of basal mudstone. Therefore, transient steady flow exists in vertical cracks
 176 during heavy rainfall, and the hydrostatic pressure triggers the detachment of rock blocks. Thus, typical scenarios (such as
 177 rainfall intensity and earthquake) need to be considered in the stability analysis model.



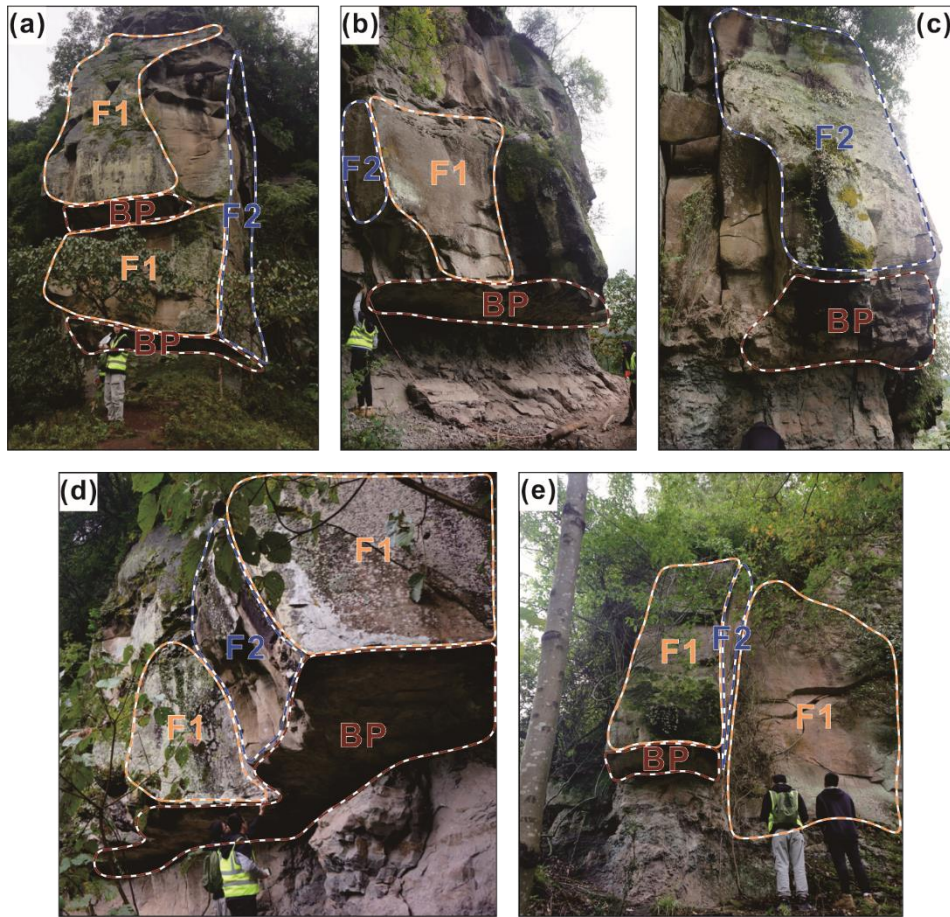
178
 179 **Figure 5** Stereo net produced using compass-clinometer survey data, which shows the densities and orientations of five clusters. The data
 180 were collected in the rockfall-prone area shown in Fig. 3d.

181 3 Calculation method

182 3.1 Geological models and assumptions

183 A detailed geological investigation of unstable rock blocks was carried out in the study area (Fig. 6). The geological model of
 184 the rock block is mainly composed of the overhanging sandstone and the underlying mudstone. The sandstone block is assumed
 185 to be a rigid body, which is divided by two sets of orthogonal vertical smooth joints without friction resistance. According to
 186 the relatively persistent sub-vertical fractures observed in the field, the vertical joints are assumed to be fully persistent in the
 187 geological model. The sandstone block is assumed to be a complete body without persistent discontinuity, and it will not
 188 disintegrate before it falls. Due to the cavity in mudstone, the contact surface between sandstone and mudstone exhibits an
 189 eccentricity effect where non-uniform stresses are distributed at different positions. Mudstone is mainly loaded by compressive
 190 stress and tensile stress. When the compressive stress of mudstone exceeds its strength on the outer side, some initial damage
 191 appears. The effective contact surface between mudstone and sandstone is reduced, which aggravates the non-uniform
 192 distribution of stress. In this way, the ability of mudstone to resist the sliding and toppling of overhanging sandstone is reduced.
 193 In the field, compression deformation of mudstone can be observed, which usually manifests as micro-fractures and cleavages

194 (Fig. 4d). The deformation is very slight and slow in the short term. In addition, the LEM is essentially a force/stress approach
195 that does not take into account the deformation. Therefore, in this study, it is assumed that the mudstone is not subjected to
196 deformation. The rock block remains in the state of static equilibrium prior to the final overall failure. Fig. 7 displays the four
197 evolution stages of biased rockfall. In the initial stage, the base cavity has not yet formed, and the normal force acting on the
198 contact surface is uniform in different positions. The eccentricity effect leads to a non-uniform supporting force as the cavity
199 grows, and partial damage gradually develops when the non-uniform stress exceeds the compressive or tensile strength of the
200 mudstone. Under the triggering effects of rainfall or earthquakes, the rock blocks are separated by sliding or toppling.

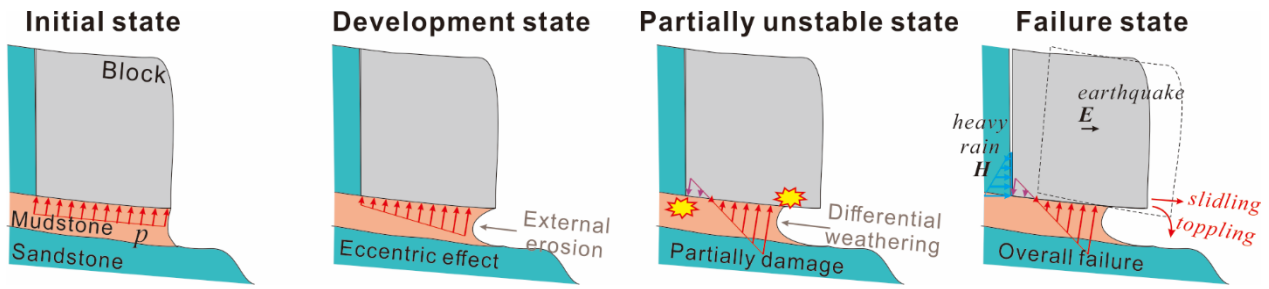


201

202 **Figure 6** The unstable blocks were labelled W02, W08, W18, W04, and W21, which are detached by the dominating discontinuities in Fig.

203 5. Basal cavities can be identified under the bedding planes of sandstone.

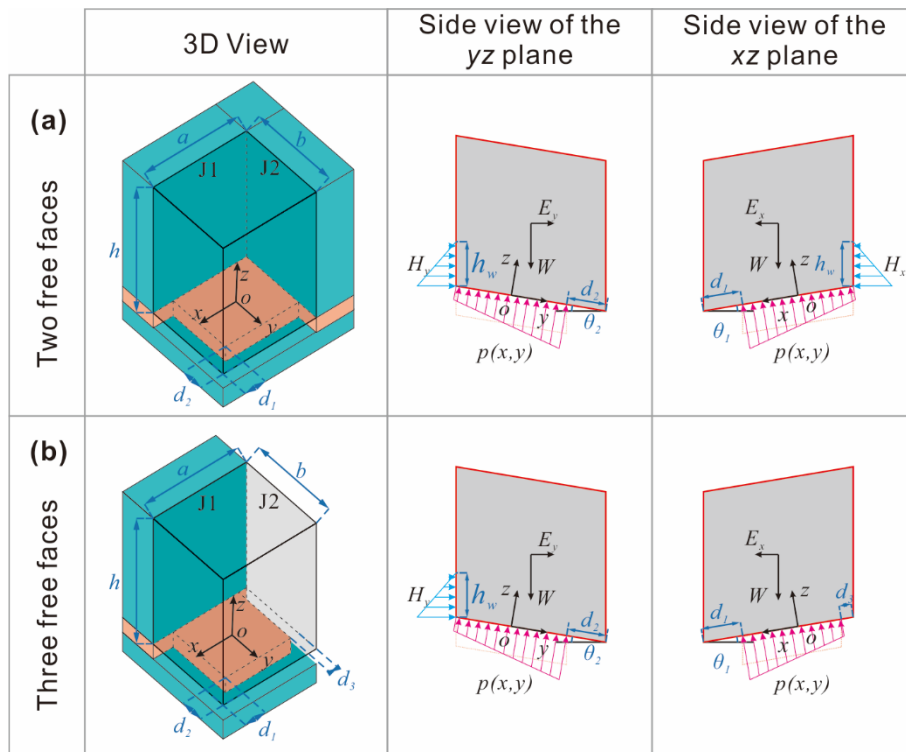
204



205
206 **Figure 7** The evolution process of rock blocks from stable state to failure.

207 Fig. 8 represents the mechanical model of the force equilibrium analysis of a rock block with two or three free faces. The rock
208 block (the overhanging sandstone) is generalized as a parallelepiped block. The underlying mudstone is impermeable, so
209 rainfall can fill the joints and transmit horizontal hydrostatic pressure. The shear strength of the underlying mudstone is
210 assumed to obey the Mohr–Coulomb criterion. Rainfall and earthquakes decrease Fos by generating hydrostatic pressure H in
211 the vertical crack and horizontal seismic force E on the block.

212 A Cartesian coordinate system is established in three-dimensional space for the force analysis. The origin O is located at the
213 centre of the contact surface between sandstone and mudstone. For the case with two free surfaces, the orientation of the free
214 surfaces is set to be the positive direction of the x -axis and y -axis. For the case with three free surfaces, the negative direction
215 of the x -axis is also a free surface. Joint J2 is perpendicular to the x -axis, and joint J1 is perpendicular to the y -axis.



216

217 **Figure 8** Diagram of the force equilibrium analysis of the rock block model. (a) and (b) represent the case of unstable rock blocks with
 218 two or three free vertical surfaces, respectively.

219 3.2 Calculation processes

220 3.2.1 Stress distribution at the block base

221 The following formulas are used to calculate the apparent dip of α (θ_1 and θ_2):

$$222 \theta_1 = \arctan(\tan \alpha \cdot \cos \omega_1) \quad (1)$$

$$223 \theta_2 = \arctan(\tan \alpha \cdot \cos \omega_2) \quad (2)$$

224 where ω_1 and ω_2 are the angles between the trend of the contact surface and the x direction or y direction, respectively.

225 As shown in Fig. 8b, with respect to the x -axis, gravity, seismic forces, and hydrostatic pressure create a non-symmetrical
 226 stress distribution on the foundation. The bending moment of gravity with respect to the x -axis (M_{bWx}) is

$$227 M_{bWx} = W \cdot \frac{d_1 - d_3}{2} \cos \theta_1 \quad (3)$$

228 Assuming that the height of the water in the fracture is h_w , the hydrostatic pressure along the x direction (H_x) and its bending
 229 moment (M_{bHx}) are respectively expressed as

$$230 H_x = \frac{\gamma_w h_w^2}{2} (b - d_2) \quad (4)$$

$$231 M_{bHx} = \int_{\frac{b-d_2}{2}}^{\frac{b-d_2}{2}} \int_0^{h_w \cos \theta_1} \gamma_w \left(h_w - \frac{z}{\cos \theta_1} \right) \left(\frac{z}{\cos \theta_1} + \frac{a - d_1 - d_3}{2} \cdot \sin \theta_1 \right) dz dy \quad (5)$$

232 The horizontal seismic force along x direction (E_x) and its bending moment (M_{bEx}) are respectively expressed as

$$233 E_x = k_e W \quad (6)$$

$$234 M_{bEx} = E_x \left(\frac{h}{2} - \frac{d_1 - d_3}{2} \sin \theta_1 \right) \quad (7)$$

235 The total applied vertical load (N_z) and the total bending moments along the x direction (M_{bx}) can be derived as

$$236 N_z = W \cos \alpha - (H_x \cdot k_1 \cdot k_3 + E_x \cdot k_2) \sin \theta_1 - (H_y \cdot k_1 + E_y \cdot k_2) \sin \theta_1 \quad (8)$$

$$237 M_{bx} = M_{bWx} + M_{bHx} \cdot k_1 \cdot k_3 + M_{bEx} \cdot k_2 \quad (9)$$

238 where k_1 , k_2 and k_3 are the coefficients set to make Eq. (8) and Eq. (9) compatible with different calculation scenarios.

239 Therefore, Eqs. (8) and (9) and the following formulas can be expressed in a unified form. In the natural scenario, k_1 and k_2

240 are both equal to 0. In the rainfall scenario, $k_1 = 1$. In the earthquake scenario, $k_2 = 1$. For the case of two free faces, $k_3 = 1$.

241 For the case of three free surfaces, $k_3 = 0$.

242 Based on bending theory ([Adrian, 2010](#)), the eccentricity distance along the x direction (e_x) can be expressed as

$$243 e_x = \frac{M_{bx}}{N_z} = \frac{M_{bWx} + M_{bHx} \cdot k_1 \cdot k_3 + M_{bEx} \cdot k_2}{W \cos \alpha - (H_x \cdot k_1 \cdot k_3 + E_x \cdot k_2) \sin \theta_1 - (H_y \cdot k_1 + E_y \cdot k_2) \sin \theta_1} \quad (10)$$

244 The same method can be used to obtain e_y :

$$245 \quad e_y = \frac{M_{by}}{N_z} = \frac{M_{bWy} + M_{bHy} \cdot k_1 + M_{bEy} \cdot k_2}{W \cos \alpha - (H_x \cdot k_1 \cdot k_3 + E_x \cdot k_2) \sin \theta_1 - (H_y \cdot k_1 + E_y \cdot k_2) \sin \theta_1} \quad (11)$$

246 According to the stress distribution of a rectangular shaped foundation ([Adrian, 2010](#)), the stress in the (x, y) coordinates,
247 $p(x, y)$, is

$$248 \quad p(x, y) = \frac{N}{A} + \frac{Ne_x}{I_y} x + \frac{Ne_y}{I_x} y \quad (12)$$

249 with the formulas

$$250 \quad I_x = \frac{(a - d_1)(b - d_2)^3}{12} \quad (13)$$

$$251 \quad I_y = \frac{(b - d_2)(a - d_1)^3}{12} \quad (14)$$

$$252 \quad A = (a - d_1 - d_3)(b - d_2) \quad (15)$$

253 By substituting Eq. (13-15) into Eq. (12), $p(x, y)$ can be derived as

$$254 \quad p(x, y) = \frac{N}{A} \left[1 + \frac{12e_x}{(a - d_1 - d_3)^2} x + \frac{12e_y}{(b - d_2)^2} y \right] \quad x \in \left[-\frac{a - d_1 - d_3}{2}, \frac{a - d_1 - d_3}{2} \right], y \in \left[-\frac{b - d_2}{2}, \frac{b - d_2}{2} \right] \quad (16)$$

255 p_{max} and p_{min} can be derived from Eq. (16) as

$$256 \quad p_{max} = p \left(\frac{a - d_1 - d_3}{2}, \frac{b - d_2}{2} \right) \quad (17)$$

$$257 \quad p_{min} = p \left(-\frac{a - d_1 - d_3}{2}, -\frac{b - d_2}{2} \right) \quad (18)$$

258 The mudstone foundation has both compressive strength and tensile strength, so the value of $p(x, y)$ is modified to obtain the
259 two piecewise functions

$$260 \quad p_p(x, y) = \begin{cases} \sigma_{cmax}, & p(x, y) \geq \sigma_{cmax} \\ p(x, y), & 0 < p(x, y) \leq \sigma_{cmax} \\ 0, & p(x, y) < 0 \end{cases} \quad (19)$$

$$261 \quad p_n(x, y) = \begin{cases} 0, & p(x, y) < -\sigma_{tmax} \\ p(x, y), & -\sigma_{tmax} \leq p(x, y) < 0 \\ 0, & p(x, y) \geq 0 \end{cases} \quad (20)$$

262 Here, $p_p(x, y)$ provides support normal force for the overhanging sandstone, and $p_n(x, y)$ provides tension force.

263 3.2.2 Calculation of factors of safety

264 According to the Mohr-Coulomb criterion, the ultimate shear strength τ_{max} is

$$265 \quad \tau_{max} = \int_{-\frac{a-d_1-d_3}{2}}^{\frac{a-d_1-d_3}{2}} \int_{-\frac{b-d_2}{2}}^{\frac{b-d_2}{2}} [p_p(x, y) \tan \varphi + c] dy dx \quad (21)$$

266 Therefore, Fos against sliding, Fos_{sl} , can be defined as

$$267 \quad FOS_{sl} = \frac{S_{stabilizing}}{S_{sliding}} = \frac{\tau_{max}}{W|\sin \alpha_s| + H_x \cdot \cos \omega_s \cdot \cos \alpha_s \cdot k_1 \cdot k_3 + H_y \cdot |\sin \omega_s| \cdot \cos \alpha_s \cdot k_1 + E \cdot \cos \alpha_s \cdot k_2} \quad (22)$$

268 When the block can slide freely, $\alpha_s = \alpha$, $\omega_s = 0$; when the block is constrained to slide along a joint plane (e.g., J1), $\alpha_s =$
 269 θ_1 or θ_2 , $\omega_s = \omega_1$ or ω_2 . For the case of an anaclinal slope, the sliding direction is opposite to the free surface. Therefore, the
 270 rock block does not slide, and FOS_{sl} is not considered in the model.

271 With regard to stability against toppling, along the x direction, the part of the block above the mudstone base provides the
 272 stabilizing moment $M_{W_{inx}}$, and the part of the block above the cavity provides the overturning moment $M_{W_{outx}}$. When tension
 273 exists, there is an additional stabilizing moment. M_{px} , $M_{W_{inx}}$, $M_{W_{outx}}$ and M_{px} can be derived as

$$274 \quad M_{W_{inx}} = W \frac{a - d_1}{a} \cos \theta_1 \cdot \left(\frac{a - d_1}{2} \right) \quad (23)$$

$$275 \quad M_{W_{outx}} = W \frac{d_1}{a} \cos \theta_1 \cdot \frac{d_1}{2} \quad (24)$$

$$276 \quad M_{px} = - \int_{\frac{b-d_2}{2}}^{\frac{b-d_2}{2}} \int_{\frac{a-d_1-d_3}{2}}^{\frac{a-d_1-d_3}{2}} p_n(x, y) \cdot \left(\frac{a}{2} - d_1 - x \right) dx dy \quad (25)$$

277 and M_{Hx} and M_{Ex} can be derived as

$$278 \quad M_{Hx} = \int_{\frac{b-d_2}{2}}^{\frac{b-d_2}{2}} \int_0^{h_w \cos \theta_1} \gamma_w \left(h_w - \frac{z}{\cos \theta_1} \right) \left(\frac{z}{\cos \theta_1} + (a - d_1) \sin \theta_1 \right) dz dy \quad (26)$$

$$279 \quad M_{Ex} = E_x \left(\frac{h}{2} + \left(\frac{a}{2} - d_1 \right) \sin \theta_1 \right) \quad (27)$$

280 Therefore, the Fos against toppling along the x direction, FOS_{tox} , results in

$$281 \quad FOS_{tox} = \frac{M_{stabilizing}}{M_{overturning}} = \frac{M_{W_{inx}} + M_{px}}{M_{W_{outx}} + M_{Hx} \cdot k_1 \cdot k_3 + M_{Ex} \cdot k_2} \quad (28)$$

282 Similarly, FOS_{toy} can be obtained as

$$283 \quad FOS_{toy} = \frac{M_{stabilizing}}{M_{overturning}} = \frac{M_{W_{iny}} + M_{py}}{M_{W_{outy}} + M_{Hy} \cdot k_1 + M_{Ey} \cdot k_2} \quad (29)$$

284 The smaller value is selected as the Fos of the toppling failure mode FOS_{to} :

$$285 \quad FOS_{to} = \min(FOS_{tox}, FOS_{toy}) \quad (30)$$

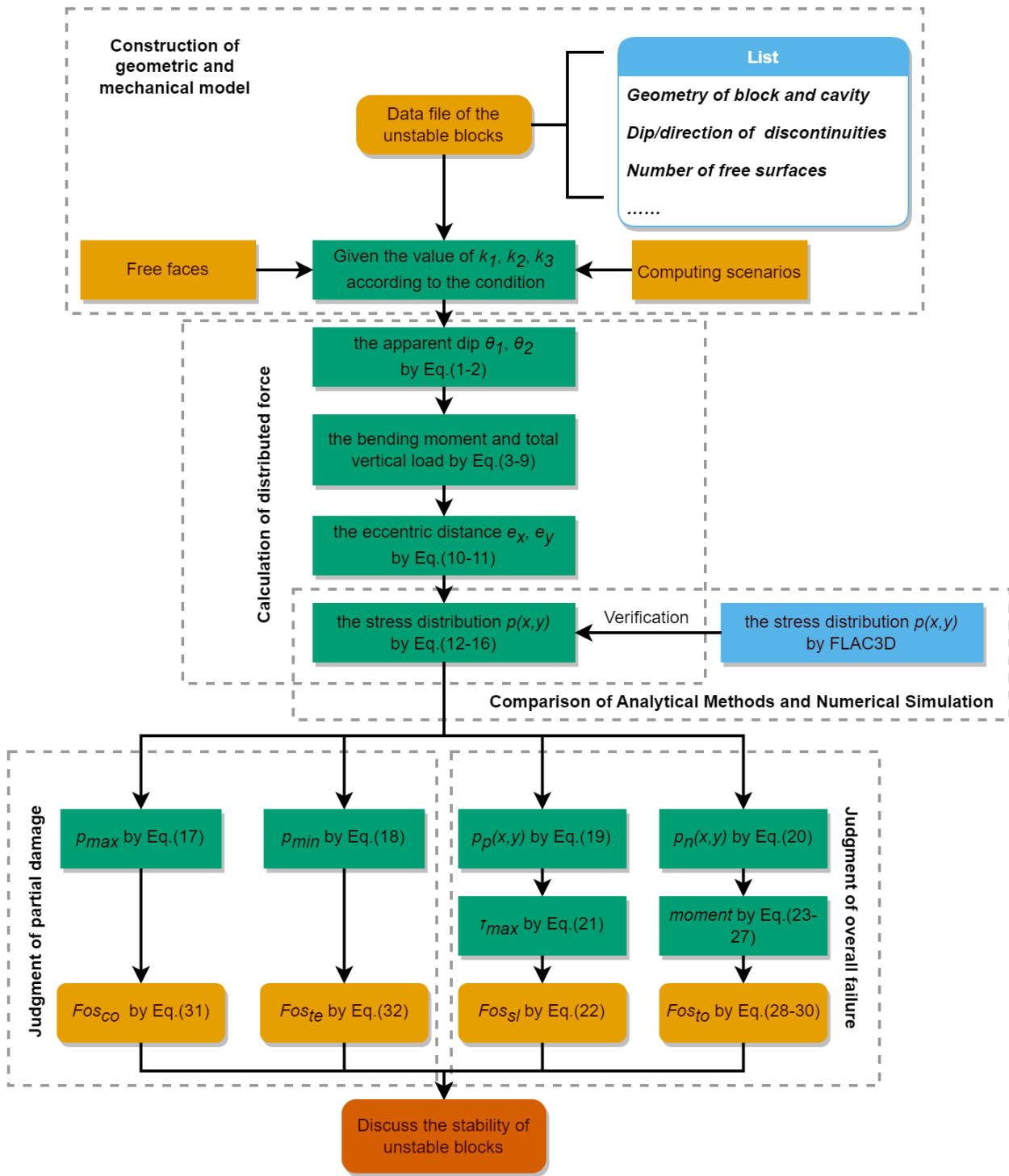
286 When the stress on mudstone exceeds its strength, it causes partial damage and decreases the stability of the rock block.

287 Therefore, Fos with the consideration of compressive strength (FOS_{co}) and tensional strength (FOS_{te}) can be derived as

$$288 \quad FOS_{co} = \frac{\sigma_{cmax}}{p_{max}} \quad (31)$$

$$289 \quad FOS_{te} = \frac{\sigma_{tmax}}{-p_{min}} \quad (32)$$

290 Fos_{co} and Fos_{te} represent the current damage degree of mudstone due to compressive stress and tensile stress, respectively.
291 When the stress exceeds the ultimate strength, the strength of the mudstone is reduced to the residual value, and the initial
292 deformation appears. The ability of mudstone to provide resistance to the sliding and toppling of sandstone blocks is thus
293 reduced, and Fos_{sl} and Fos_{to} subsequently decline. The smaller the value of Fos_{co} and Fos_{te} , the greater the damage to the
294 underlying mudstone. The effective contact area between sandstone and mudstone becomes smaller as the development of
295 compressive and tension damage, which significantly affects the stability of the overhanging sandstone block.
296 Finally, four Fos of unstable rock block are obtained. Fos_{sl} and Fos_{to} are routine indicators directly representing the stability
297 of sandstone blocks. Fos_{co} and Fos_{te} are two indicators proposed in this study for the stability analysis of biased rockfall,
298 which describe the damage state of the underlying mudstone base. It is necessary to simultaneously consider four Fos to
299 evaluate the stability of unstable biased rockfall. The entire calculation process is shown in Fig. 9.
300

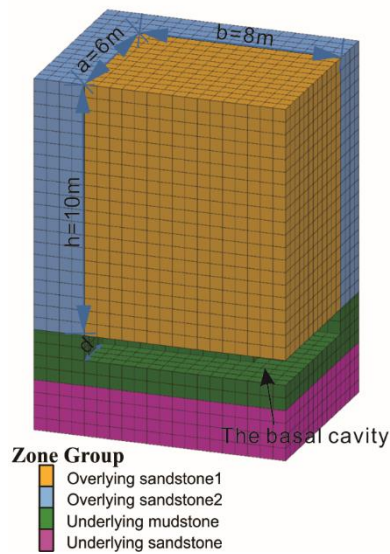


301
302

Figure 9 Calculation process of Fos of the unstable rock blocks.

303 **4 Validation of analytical methods by numerical simulation**

304 The damage mechanisms at the base of the rock block play an important role in the rockfall evolution process. However, the
305 stress distribution on the contact surface calculated by the proposed analytical methods is difficult to be validated by the field
306 data. Therefore, numerical simulation of a biased rockfall was conducted in this study to determine the stress distribution on
307 the contact surface between overhanging sandstone and underlying mudstone. By comparing the results of the proposed
308 analytical methods with those obtained from the numerical simulation, the reliability of the analytical methods can be validated.
309 FLAC3D, a professional software that utilizes the finite difference method (FDM) for three-dimensional analysis of rocks,
310 soils, and other materials, was employed for the 3D numerical simulation. Based on the geological models, a 3D numerical
311 simulation model was conducted with FLAC3D 6.00 to analyse the stress distribution on the contact surface (Fig. 10).



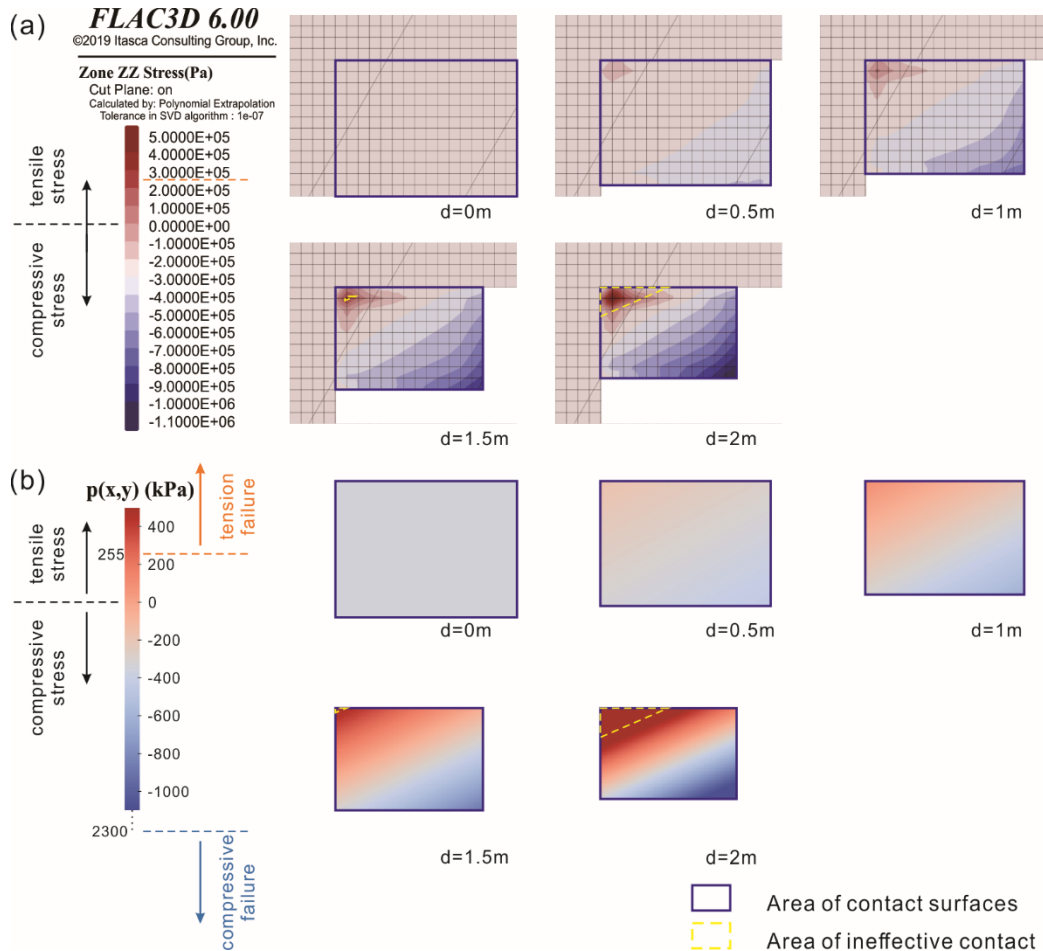
312

313

Figure 10 Numerical model built in FLAC3D

314 The model is mainly composed of sandstone and mudstone, which the Overhanging sandstone1 represents a unstable rock
315 block (dimensions $a \times b \times h$ are 6m, 8m, 10m respectively) , and the weathering process of the cavity is represented by excavating
316 in stages in the underlying mudstone. Sandstone was considered as elastic model, and mudstone was assigned Mohr-Coulomb
317 model. Material properties were determined by referring to published literature and investigation reports in the study area. The
318 unit weight of the sandstone block (γ_s) is 25 kN/m³ (Tang et al., 2010), and the mudstone is 22.54 kN/m³. The friction angle
319 of the contact surface (ϕ) is set to 25° and the cohesion (c) is set to 70 kPa (Zhang et al., 2016). Because of the strength
320 degradation of mudstone foundations due to intense weathering, the maximum compressive stress of mudstone (σ_{cmax}) is
321 replaced by the bearing capacity of mudstone foundations (2300 kPa), which is obtained through plate load tests in adjacent
322 areas (Zheng et al., 2021). In addition, the maximum tensile stress of mudstone (σ_{tmax}) is valued as one-ninth of σ_{cmax} .
323 The west, north and bottom boundaries of the model are constrained by roller boundary conditions. The cohesion and internal
324 friction angle of the interface between Overhanging sandstone1 and Overhanging sandstone2 are set to 0. After reaching the

325 initial force-equilibrium state, the mudstone was excavated to simulate the weathering process, and the vertical stress
 326 distribution on the sand-mudstone interface at different cavity depths was obtained, as shown in Figure 11.



327

328 **Fig.11** Diagram of stress distribution in the vertical direction on the contact interface through different methods, (a) the
 329 results of numerical simulation by FLAC3D, (b) the results of of proposed analytical method.

330 When there is no cavity present, represented by d=0m, the stress distribution is uniform compressive stress (According to the
 331 FLAC3D software, compressive stresses are negative). At d=0.5m, the stress remains entirely compressive, but non-uniform
 332 stress distribution occurs on the contact surfaces. At d=1m, the vertical stress value in the upper left corner of the contact
 333 interface surpasses 0 (Fig.11), indicating the presence of tensile stress. As d increases to 1.5m or 2m, the tensile stress in the
 334 upper left corner gradually intensifies, exacerbating the non-uniform stress distribution. The results obtained from the
 335 numerical simulation align with those from the analytical method, confirming the existence of tensile stress at the contact
 336 interface in the biased rockfall due to external erosion development (Fig.11). Tensile stress commonly emerges within the
 337 contact surface, making it challenging to observe directly in the field.

338

339 In the context of the limit equilibrium method, the contact area plays a vital role in stability analysis, as shown in Eq. (21)-(30)
340 in Section 3. The numerical simulation process provides an intuitive understanding of the influence of non-uniform stress
341 distribution on the contact surfaces on the stability of rock blocks. Whether subjected to tension or compression, the rock layer
342 has an ultimate strength. In Fig.11, when $d=1.5\text{m}$ or 2m , the tensile stress exceeds the ultimate tensile strength, leading to
343 tensile failure in the upper left corner of the stress distribution diagram. The region enclosed by a yellow dotted line represents
344 ineffective contact, where no anti-slip force or overturning moment can be generated due to tension failure at the contact
345 surface. Therefore, this area needs to be subtracted from the total contact area when calculating $[\text{Fos}]_{\text{-sl}}$ and $[\text{Fos}]_{\text{-to}}$.
346 Similar situations occur when the compressive stress exceeds the ultimate compressive strength. The current maximum
347 compressive stress has not reached the ultimate compressive strength in Figure 11. However, As d continues to increase, the
348 area of compression failure will appear in the lower right corner of diagram in Figure 11. This occurrence diminishes the area
349 capable of providing anti-slip force or overturning moment, thereby reducing the stability of the rock blocks.
350 The traditional LEM method does not account for distributed forces and fails to consider changes in the contact surface. The
351 method proposed in this study addresses this issue and is applied to the calculation of the $[\text{Fos}]_{\text{-sl}}$ and $[\text{Fos}]_{\text{-toas}}$
352 presented in Eq. (21), (25) and (26)).

353 **5 Results**

354 A detailed field investigation was carried out in the source area of rockfall (Fig. 3d). The size of the blocks was determined by
355 on-site measurement with tape and a laser rangefinder. The basal cavities in mudstone were measured with a steel ruler, and
356 the morphological characteristics of mudstone foundation were mainly described with the average erosion depth of the cavity.
357 The attitude of discontinuities was measured by compass. The mechanical parameters have been given in Section.4. The height
358 of the water level (h_w) is set to be one-third of h , and an earthquake contribution coefficient k_e of 0.05 is considered in stability
359 calculations. The data obtained from the field survey were organized according to the coordinate system of the geological
360 model in Section 3.1, and Fos was calculated according to the calculation steps in Section 3.2. The calculated geometric
361 parameters and Fos results are shown in Table 2.

Table 2 Geometric parameters of rock blocks in the study area and Fos results.

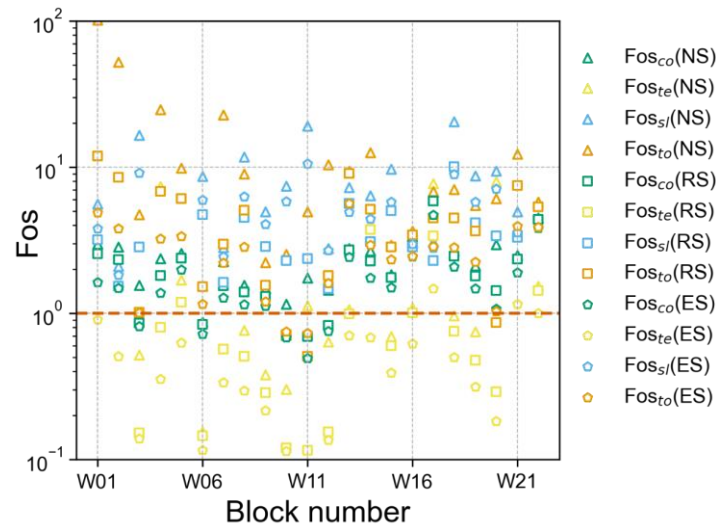
Block number	Free faces	h [m]	a [m]	b [m]	d_1 [m]	d_2 [m]	d_3 [m]	α [°]	Dip direction [°]			NS (Natural scenario)			RS (Rainfall scenario)			ES (Earthquake scenario)						
									BD	J1	J2	Fos_{te}	Fos_{co}	Fos_{st}	Fos_{to}	Fos_{min}	Fos_{te}	Fos_{co}	Fos_{st}	Fos_{to}	Fos_{te}	Fos_{co}	Fos_{st}	Fos_{to}
W01	3	23	7.2	6.1	0.65	0.25	0.17	6	78	7	97	-	2.99	5.61	101.54	2.99	-	2.56	3.18	11.91	0.90	1.63	3.81	4.88
W02	3	23	6.42	5.25	0.78	0.4	0.31	16	148	51	141	-	2.84	2.10	52.28	2.10	-	2.33	1.54	8.49	0.51	1.48	1.82	3.79
W03	2	20	3.5	2.6	0.84	0.55	-	7	341	53	143	0.52	1.56	16.53	4.72	0.52	0.15	0.86	2.83	1.02	0.14	0.81	9.12	1.01
W04	2	19	4.6	4.6	0.62	0.77	-	7	273	65	155	7.35	2.37	-	24.74	2.37	0.80	1.81	-	6.83	0.35	1.38	-	3.23
W05	2	15	16.7	5.6	2.13	1.36	-	5	283	50	140	1.70	2.57	-	9.86	1.70	1.19	2.39	-	6.10	0.63	1.99	-	3.36
W06	3	20	16.7	9.7	7.5	4.2	3.9	5	302	226	316	0.15	0.87	8.67	1.53	0.15	0.15	0.84	4.73	1.52	0.12	0.72	5.96	1.16
W07	2	22	9.2	3.7	0.64	0.8	-	12	324	315	405	-	2.27	2.82	22.86	2.27	0.57	1.55	1.62	2.97	0.34	1.28	2.44	2.21
W08	2	23	12	7.9	2	1.9	-	3	317	332	422	0.76	1.55	11.75	8.99	0.76	0.51	1.40	4.51	5.09	0.29	1.14	6.29	2.84
W09	2	18	8.4	6	0.9	2.5	-	8	60	335	425	0.38	1.48	4.98	2.23	0.38	0.29	1.30	2.87	1.56	0.22	1.12	4.08	1.20
W10	2	23	5.7	3.3	1.3	0.85	-	5	329	313	403	0.30	1.16	7.41	2.53	0.30	0.12	0.71	2.30	0.71	0.11	0.68	5.84	0.75
W11	3	22	1.1	2	0.1	0.64	0.1	4	327	120	210	1.13	1.74	19.08	4.97	1.13	0.12	0.69	2.37	0.51	0.07	0.49	10.57	0.73
W12	2	25	3.9	4	0.74	0.96	-	12	355	297	387	0.64	1.44	2.78	10.36	0.64	0.15	0.82	1.48	1.81	0.14	0.75	2.70	1.61
W13	2	12	11.9	10.9	3	2.28	-	7	36	73	163	1.06	2.77	7.28	9.39	1.06	0.99	2.71	5.63	9.02	0.70	2.41	4.93	5.65
W14	3	19	13	5	0	1.1	0	8	296	73	163	-	2.67	6.40	12.57	2.67	3.75	2.28	3.09	5.15	0.68	1.75	4.41	2.94
W15	2	18	22	6	8.3	0	-	8	351	200	290	0.70	1.84	9.74	2.93	0.70	0.60	1.75	5.03	2.83	0.39	1.50	5.79	2.34
W16	3	11	5.2	7.6	0	2.9	0	13	42	144	234	1.09	3.04	3.46	3.65	1.09	1.01	2.96	2.84	3.45	0.62	2.45	2.98	2.45
W17	3	7	8	2	0	0.56	0	20	30	156	246	7.71	6.72	3.07	6.83	3.07	3.40	5.87	2.29	4.49	1.48	4.70	2.81	2.86
W18	2	12	8.5	4.5	1.61	1.27	-	2	252	253	343	0.97	2.66	20.49	7.05	0.97	0.75	2.46	10.06	4.50	0.50	2.08	8.90	2.82
W19	2	15	4.2	5.2	1.6	0.68	-	5	28	56	146	0.75	2.12	8.71	5.49	0.75	0.48	1.80	4.17	3.66	0.31	1.48	5.79	2.24
W20	3	15	1.8	1.7	0.23	0.5	0.3	4	20	63	153	7.96	2.95	9.44	6.08	2.95	0.29	1.43	3.39	0.87	0.18	1.07	7.12	1.03
W21	3	20	18.9	9	0	2	0	7	348	71	161	-	2.51	4.96	12.25	2.51	-	2.36	3.31	7.48	1.15	1.90	3.58	3.95
W22	2	7	5.4	5.7	1	1.65	-	6	294	53	143	1.53	4.48	-	5.78	1.53	1.44	4.38	-	5.37	1.00	3.81	-	3.88

Note: When there is no tensile stress in the mudstone foundation, Fos_{te} has no value. For the case of an anacinal slope, blocks do not slide and Fos_{st} has no value. Both parameters are replaced by "-".

363 6 Discussion

364 6.1 Characteristics of rock block stability

365 There are up to 12 results of Fos per potential unstable block with the consideration of three scenarios and four failure modes
366 (i.e., partial damage and overall failure). Most Fos_{te} values are less than 1 in all scenarios (yellow points in Fig.12), except
367 for two blocks (i.e., W17 and W20), whose Fos_{te} values are also close to 1 under rainfall or earthquake scenarios. Although
368 most of Fos_{co} values (green points in Fig. 12) are greater than 1, they are closer to the critical state of $Fos = 1$ than Fos_{sl} and
369 Fos_{to} (represented by blue and orange points in Fig. 12, respectively). The compression damage of the exposed mudstone can
370 be investigated in the field survey (Fig. 4d). However, it is difficult to observe the phenomenon of tensile damage inside the
371 mudstone base. In the case of weak tensile strength, the mudstone base suffers from tensile failure, and compression failure
372 usually occurs before tension failure. According to the results, their Fos_{te} and Fos_{co} are less than 1 or close to 1, which means
373 that the underlying mudstone has been partially damaged due to slight compressive or tensile failure, and the blocks are
374 potentially unstable with the current depth of the basal cavity. However, most of the blocks do not exhibit overall failure, and
375 they still exist on the slope. Moreover, their Fos_{sl} and Fos_{to} values are greater than 1 in different scenarios, which is consistent
376 with this actuality. The results indicate that most of the blocks are close to a critical state, in which they are partially damaged
377 but the whole block is still stable.



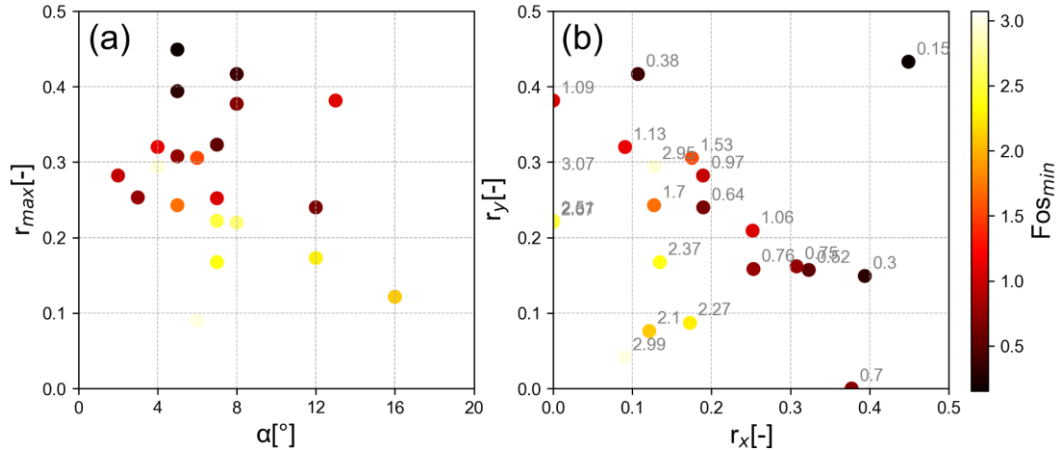
378

379 **Figure 12** Distribution of Fos in different scenarios. Shapes represent different scenarios and colours represent different failure modes.

380 6.2 Relationship between Fos and geometric parameters

381 Fig. 13 presents the relationship between Fos_{min} and two main geometric parameters, the dip of the contact surface and the
382 retreat ratio. In general, the dip angle of the contact surface (α) is the key factor influencing the sliding failure mode. The

383 horizontal axis in Fig. 13a is α between the rock blocks and underlying mudstone. Most of the points in Fig. 13a are in the
 384 interval $[0, 8^\circ]$, which is consistent with the features of sub-horizontal strata in the study area. The shade of the points does not
 385 change significantly in the x -axis direction, as Fig. 13a shows. Therefore, compared with the maximum retreat ratio (r_{max}),
 386 the dip of the contact surface has less influence on rockfall stability in the study area. There was a significant positive
 387 correlation between the retreat ratio (r_{max}) and Fos_{min} . In Fig. 13b, as the retreat ratios increase in the positive direction of
 388 the x -axis and y -axis, the rock blocks show a notable tendency to be unstable.



389
 390 **Figure 13** Correlation between Fos and the dip of contact surface and retreat ratio. Here, α is the dip angle of the contact surface between
 391 rock block and underlying mudstone, r_x and r_y are the retreat ratio along x direction and y direction, respectively, equal to d_1/a and d_2/b ,
 392 and r_{max} is the larger of r_x and r_y .

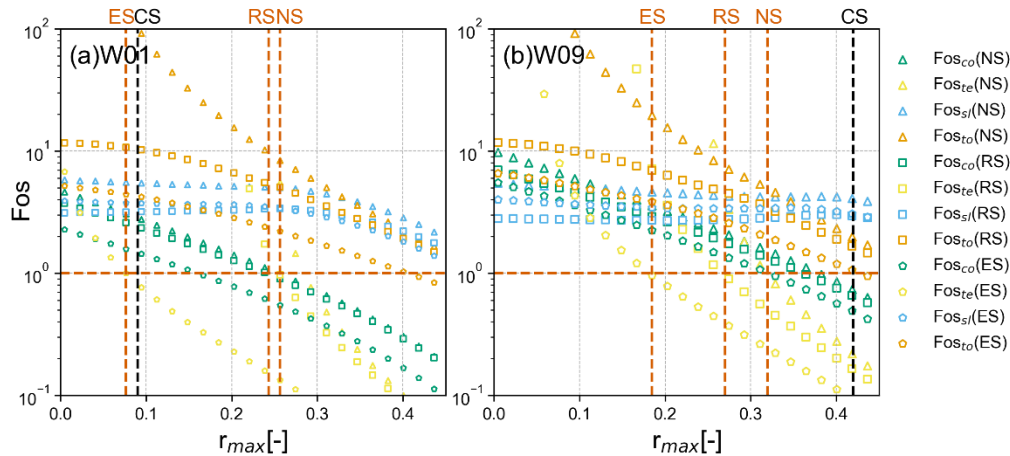
393 6.3 Definition of rockfall susceptibility

394 To explore the variation in Fos with the progressive erosion process of the cavity on the blocks, the cavity retreat velocities in
 395 different directions are assumed to be equal (5 mm/year, Zhang et al. (2016)). Fig. 14 shows the variations in Fos of two
 396 specific blocks during the evolution process of the mudstone cavity. In the initial stage, the cavity is small, and the overhanging
 397 block is stable; all Fos values are greater than 1.0. The cavity expands over time as the mudstone weathers; then, the contact
 398 area decreases, and non-uniform distributed stress arises. When the stress exceeds the ultimate strength of mudstone in a partial
 399 area, Fos_{co} and Fos_{te} decrease significantly, as shown in Fig. 14. The instability of the blocks starts from the failure (or
 400 damage) of the foundation. Fos_{te} and Fos_{co} reach the critical state much earlier than Fos_{sl} and Fos_{to} . For these two specific
 401 blocks, when r_{max} increases to 0.4, Fos_{sl} and Fos_{to} are still higher than 1.0. This means that the rock blocks can remain
 402 globally stable in this condition.

403 These results further elucidate the stability analysis model proposed in this study. Fos_{co} and Fos_{te} introduced in this model
 404 present the damage state of basal mudstone caused by compressive and tensile stresses, which do not provide global instability
 405 of the overhanging block as sliding and toppling. However, Fos_{co} and Fos_{te} are important preliminary signs of subsequent

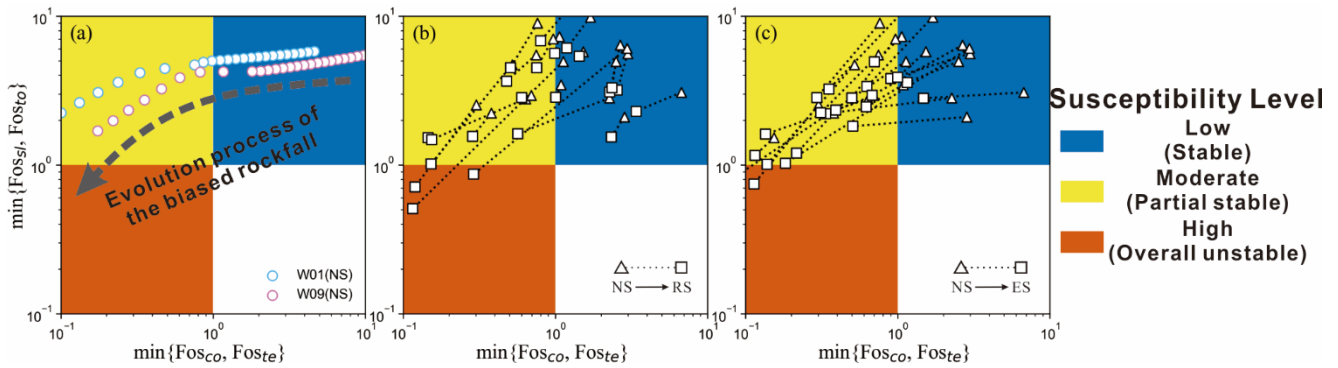
406 global failure of the rock block, as presented through the numerical simulation in Section 4. The damage in the basal mudstone
 407 can significantly accelerate weathering and prompt expansion of the cavity, which will lead to global failure. The lower Fos_{co}
 408 and Fos_{te} are, the lesser the safety margin of the blocks. Therefore, the four Fos used in this study can provide a more
 409 comprehensive quantification of rockfall stability.

410 This result is consistent with Fig. 12, in which 63.7% of the yellow and green points (Fos_{te} and Fos_{co}) are located between
 411 $Fos = 0.7$ and $Fos = 2.0$. This result can be validated by the field phenomena. In the study area, rock damage (e.g., micro-
 412 fractures and cleavages) can be observed in the underlying mudstone. However, most overhanging rock blocks are stable at
 413 the present time. This means that even if Fos_{sl} or Fos_{to} is higher than 1, its foundation has begun to be damaged. In the case
 414 of heavy rain or earthquakes, Fos_{sl} and Fos_{to} may be reduced to less than 1, and the rockfall occurs.



415
 416 **Figure 14** Variation in Fos with r_{max} . (a) and (b) are the results for W01 and W09, respectively, which represent the situation of the blocks
 417 with two and three free faces. The black dotted line (CS) approximately represents the current state of the unstable blocks. The red dotted
 418 lines correspond to the critical values of r in different scenarios.

419 Based on the meaning of four Fos , rockfall susceptibility can be divided into three levels. When both Fos_{co} and Fos_{te} are
 420 greater than 1, the overall rock block is stable, and the mudstone base is not damaged, which is defined as “low susceptibility”
 421 and represented by the blue area in Fig. 15. With the development of cavity erosion, when Fos_{co} or Fos_{te} is less than 1 and
 422 Fos_{sl} and Fos_{to} are higher than 1, the base undergoes be damaged, and the overhanging sandstone blocks remain relatively
 423 stable. This state is defined as “moderate susceptibility” and represented by the yellow area. When Fos_{sl} or Fos_{to} is less than
 424 1 in some scenarios, the rock blocks are in a “high susceptibility” state, which means that rockfalls are highly likely to occur.
 425 Fig. 15a indicates that along with the increase in the cavity retreat ratio, the susceptibility of W01 and W09 changes from low
 426 susceptibility to moderate susceptibility in the natural scenario. As Fig. 15b and c show, when rainfall or earthquake occurs,
 427 Fos_{sl} or Fos_{to} of some blocks is less than 1, which means that some blocks have evolved to the state of high susceptibility
 428 and the overall sandstone blocks are unstable.

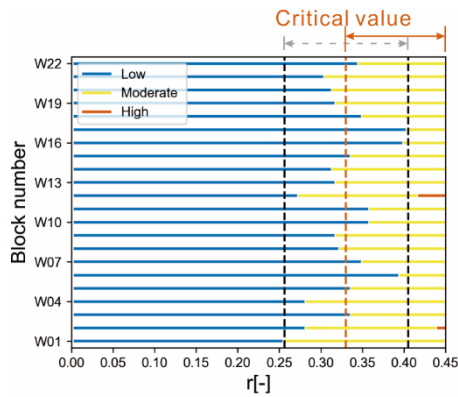


429

430 **Figure 15** Rockfall susceptibility based on the combination of four Fos . The susceptibility is defined as three levels, represented by red,
 431 yellow and blue. (a) shows the progressive failure process of the rock block changing from low susceptibility to moderate susceptibility as
 432 the cavity retreat ratio increases (illustrated by W01 and W09 in the natural scenario). (b) and (c) show the change in susceptibility of biased
 433 rock blocks, when the scenario changes from natural conditions to rainfall and earthquake conditions.

434 6.4 Critical retreat ratio in the study area

435 The cavity plays an important role in the progressive failure process of biased rockfall. To analyse the effect of the retreat ratio
 436 on the stability of rock blocks, all blocks in the study area were selected to calculate their Fos and susceptibility level with the
 437 increasing r , whose retreat velocities in different directions are assumed to be equal. Fig. 16 shows that along with the increase
 438 in the retreat ratio, the susceptibility level of rock blocks changes from low to moderate susceptibility. Corresponding to the
 439 critical state of $\min \{Fos_{co}, Fos_{te}\} = 1$ of all blocks, the minimum retreat ratio is 0.26, and the maximum retreat ratio is 0.41,
 440 as marked by the vertical black dotted line in Fig. 16. According to the statistical analysis of critical retreat ratios, both mean
 441 and median are 0.33. Therefore, the critical retreat ratio of the rock blocks in the study area can be determined as 0.33, which
 442 is marked by the vertical red dotted line in the Fig. 16. The critical retreat ratio calculated by this method can be used for the
 443 preliminary identification of potential unstable rock blocks in a specific area, which can help concentrate limited risk treatment
 444 resources on these priorities. It should be emphasized that the mechanical parameters and analysis scenarios significantly affect
 445 the critical value. Therefore, the elaborative risk control of a given rockfall should be arranged based on its specific parameters
 446 and analysis scenarios.



447

448 **Figure 16** Effect of the retreat ratio (r) on the Fos of the rock block, which is illustrated by all blocks in the study area.

449 6.5 Limitations

450 This study involves the development of an analytical model for the three-dimensional stability of biased rockfall, combining
 451 the basic LEM method and the consideration of the eccentricity effect. Due to the complexity of rock structure and force
 452 analysis, it is necessary to highlight the limitations of this model.

453 First, this study uses a three-dimensional coordinate system and bending theory. It is difficult to consider diverse shapes of
 454 rock blocks, and the rock block was simplified as a prismatic column. The assumption of fully persistent discontinuities may
 455 underestimate the stability of rock blocks, and ignores the stress transmission in joints or rock bridges. Then, following the
 456 basic framework of the general LEM method, this study assumed that the rock is not subjected to deformations. The complete
 457 stress–strain behaviour, such as the deformation in the mudstone layer, is not considered in this study. The mode of tension
 458 failure is very difficult to observe in the field, and it is currently verified by means of numerical simulation. Furthermore, the
 459 block stability is strongly influenced by the uncertainty of mechanical parameters. However, because of the difficulties in
 460 sampling strongly weathered mudstone, it is difficult to obtain adequate parameter values for uncertainty statistics. These
 461 limitations will be important considerations in future studies.

462 7 Conclusion

463 Due to differential weathering in sub-horizontally interbedded of hard rock and soft rock, multi-layer biased rockfalls develop
 464 on steep slopes. In mountainous ranges, cut slopes, and coastal cliffs, rockfall may cause significant facility damage and
 465 casualties in residential areas and transport corridors. The aim of this study was to present a new three-dimensional analytical
 466 method for the stability of rock blocks with basal cavities. In this method, a non-uniform distributed stress due to the
 467 eccentricity effect is applied at the contact surface instead of a point force. The development of non-uniform distributed stress
 468 calculated by the proposed analytical methods was validated by numerical simulation, which presents the evolution process of
 469 biased rockfall from partial damage of the soft underlying layer, caused by non-uniform distributed stress, to toppling and

470 sliding of overhanging hard rock block due to overall unbalanced force. The method considers four failure modes according
471 to the rockfall evolution process, including partial damage of the soft foundation (Fos_{co} and Fos_{te}) and overall failure of the
472 rock block (Fos_{sl} and Fos_{to}).

473 Taking the northeast edge of the Sichuan Basin in Southwest China as the study area, the proposed method is used to calculate
474 the Fos of biased unstable rock blocks. The results show that in the natural scenario, the underlying mudstone of some rock
475 blocks has been partially damaged, and compression failure of the mudstone has been observed in the field. Some rock blocks
476 are expected to fail as a whole in rainfall or earthquake scenarios. The statistical analysis indicates that the retreat ratio is the
477 crucial factor influencing the Fos of biased rockfall. On the basis of different combinations of four Fos , rockfall susceptibility
478 was classified into three levels. As the retreat rate increases, the rock blocks undergo an evolution process from stability to
479 partial instability and then overall instability. Based on the current mechanical parameters of the eastern Sichuan Basin, the
480 critical retreat ratio from low to moderate rockfall susceptibility is 0.33.

481 The proposed method improves the three-dimensional mechanical model of a rock block with a basal cavity by considering
482 non-uniform distributed stress at the contact surface, which could promote the accuracy of rockfall stability analysis. Due to
483 the assumptions adopted and the complexity of the failure mechanism of biased rockfall, there are some limitations in this
484 method, mainly including the simplification of boundary conditions and rock deformation. These limitations will be important
485 considerations in future studies.

486 **Data availability**

487 All raw data can be provided by the corresponding authors upon request.

488 **Author contributions**

489 XS, BC and JD planned the campaign; XS and BC performed the field measurements; XS, BC, WW and BL designed and
490 developed the methodology. XS, BC and JD analysed the data; XS and BC wrote the manuscript draft; JD and WW reviewed
491 and edited the manuscript.

492 **Competing interests**

493 The authors declare that they have no conflicts of interest.

494 **Acknowledgements**

495 This research is funded by the National Natural Science Foundation of China (No. 42172318 and No. 42177159). The first
496 author thanks Master Chengjie Luo and Yu Wang for data collection in the field. We also appreciate the assistance of the
497 Research Center of Geohazard Monitoring and Warning in the Three Gorges Reservoir, China.

498 **References**

- 499 Adrian, I.: Pressures distribution for eccentrically loaded rectangular footings on elastic soils, Proceedings of the 2010
500 international conference on Mathematical models for engineering science, Tenerife, Spain, 213–216,
- 501 Alejano, L. R., Carranza-Torres, C., Giani, G. P., and Arzua, J.: Study of the stability against toppling of rock blocks with
502 rounded edges based on analytical and experimental approaches, Eng. Geol., 195, 172-184,
503 <https://doi.org/10.1016/j.enggeo.2015.05.030>, 2015.
- 504 Alejano, L. R., Ordóñez, C., Armesto, J., and Rivas, T.: Assessment of the instability hazard of a granite boulder, Nat. Hazards,
505 53, 77-95, <https://doi.org/10.1007/s11069-009-9413-0>, 2010.
- 506 Ashby, J.: Sliding and toppling modes of failure in models and jointed rock slopes, M.S. thesis, Imperial College London
507 University, London, 1971.
- 508 Bray, J. W. and Goodman, R. E.: The theory of base friction models, Int. J. Rock Mech. Min. Sci. Geomech. Abstr., 18, 453-
509 468, [https://doi.org/10.1016/0148-9062\(81\)90510-6](https://doi.org/10.1016/0148-9062(81)90510-6), 1981.
- 510 Budetta, P.: Assessment of rockfall risk along roads, Nat. Hazards Earth Syst. Sci., 4, 71-81, [https://doi.org/10.5194/nhess-4-](https://doi.org/10.5194/nhess-4-71-2004)
511 [71-2004](https://doi.org/10.5194/nhess-4-71-2004), 2004.
- 512 Budetta, P. and Nappi, M.: Comparison between qualitative rockfall risk rating systems for a road affected by high traffic
513 intensity, Nat. Hazards Earth Syst. Sci., 13, 1643-1653, <https://doi.org/10.5194/nhess-13-1643-2013>, 2013.
- 514 Chau, K. T., Wong, R. H. C., Liu, J., and Lee, C. F.: Rockfall hazard analysis for Hong Kong based on rockfall inventory,
515 Rock Mech. Rock Eng., 36, 383-408, <https://doi.org/10.1007/s00603-002-0035-z>, 2003.
- 516 Chen, H. K. and Tang, H. M.: Stability analysis method of perilous rock in source of avalanche, J. Geol. Min. Res., 2, 60-67,
517 <https://doi.org/10.5897/JGMR.9000070>, 2010.
- 518 Chen, H. K., Xian, X. F., Tang, H. M., and Feng, Q. H.: A massive development mechanism and countermeasures for perilous
519 rocks in the Three Gorges Reservoir area of PR China: The example of the Taibaiyan cliff at Wanzhou, Journal of Chongqing
520 University, 31, 1178-1184, <https://doi.org/10.11835/j.issn.1000-582X.2008.10.019>, 2008.
- 521 Corominas, J., Mavrouli, O., and Ruiz-Carulla, R.: Magnitude and frequency relations: are there geological constraints to the
522 rockfall size?, Landslides, 15, 829-845, <https://doi.org/10.1007/s10346-017-0910-z>, 2018.
- 523 Cruden, D. M. and Varnes, J. D.: Landslide types and processes. Landslides: investigation and mitigation, transportation
524 research board (National Research Council), National Academy Press, Washington, DC, 1996.

525 D'Amato, J., Hantz, D., Guerin, A., Jaboyedoff, M., Baillet, L., and Mariscal, A.: Influence of meteorological factors on
526 rockfall occurrence in a middle mountain limestone cliff, *Nat. Hazards Earth Syst. Sci.*, 16, 719-735,
527 <https://doi.org/10.5194/nhess-16-719-2016>, 2016.

528 Derron, M. H., Jaboyedoff, M., and Blikra, L. H.: Preliminary assessment of rockslide and rockfall hazards using a DEM
529 (Oppstadhornet, Norway), *Nat. Hazards Earth Syst. Sci.*, 5, 285-292, <https://doi.org/10.5194/nhess-5-285-2005>, 2005.

530 Ferrari, F., Giacomini, A., and Thoeni, K.: Qualitative Rockfall Hazard Assessment: A Comprehensive Review of Current
531 Practices, *Rock Mech. Rock Eng.*, 49, 2865-2922, <https://doi.org/10.1007/s00603-016-0918-z>, 2016.

532 Frattini, P., Crosta, G., Carrara, A., and Agliardi, F.: Assessment of rockfall susceptibility by integrating statistical and
533 physically-based approaches, *Geomorphology*, 94, 419-437, <https://doi.org/10.1016/j.geomorph.2006.10.037>, 2008.

534 Frayssines, M. and Hantz, D.: Modelling and back-analysing failures in steep limestone cliffs, *Int. J. Rock Mech. Min. Sci.*,
535 46, 1115-1123, <https://doi.org/10.1016/j.ijrmms.2009.06.003>, 2009.

536 Guzzetti, F., Reichenbach, P., and Wieczorek, G. F.: Rockfall hazard and risk assessment in the Yosemite Valley, California,
537 USA, *Nat. Hazards Earth Syst. Sci.*, 3, 491-503, <https://doi.org/10.5194/nhess-3-491-2003>, 2003.

538 Hutchinson, J. N.: Field and laboratory studies of a fall in Upper Chalk cliffs at Joss Bay, Isle of Thanet, in: *Stress-Strain*
539 *Behaviour of Soils*, Proceedings of the Roscoe Memorial Symposium, Oxfordshire, 29-31 March 1971, 692-706, 1972.

540 Jaboyedoff, M., Baillifard, F., Philippossian, F., and Rouiller, J. D.: Assessing fracture occurrence using "weighted fracturing
541 density": a step towards estimating rock instability hazard, *Nat. Hazards Earth Syst. Sci.*, 4, 83-93,
542 <https://doi.org/10.5194/nhess-4-83-2004>, 2004.

543 Jaboyedoff, M., Ben Hammouda, M., Derron, M.-H., Guérin, A., Hantz, D., and Noel, F.: The Rockfall Failure Hazard
544 Assessment: Summary and New Advances, in: *Understanding and Reducing Landslide Disaster Risk: Volume 1 Sendai*
545 *Landslide Partnerships and Kyoto Landslide Commitment*, edited by: Sassa, K., Mikoš, M., Sassa, S., Bobrowsky, P. T.,
546 Takara, K., and Dang, K., Springer International Publishing, Cham, 55-83, https://doi.org/10.1007/978-3-030-60196-6_3,
547 2021.

548 Kogure, T., Aoki, H., Maekado, A., Hirose, T., and Matsukura, Y.: Effect of the development of notches and tension cracks
549 on instability of limestone coastal cliffs in the Ryukyus, Japan, *Geomorphology*, 80, 236-244,
550 <https://doi.org/10.1016/j.geomorph.2006.02.012>, 2006.

551 Kromer, R., Lato, M., Hutchinson, D. J., Gauthier, D., and Edwards, T.: Managing rockfall risk through baseline monitoring
552 of precursors using a terrestrial laser scanner, *Can. Geotech. J.*, 54, 953-967, <https://doi.org/10.1139/cgj-2016-0178>, 2017.

553 Malamud, B. D., Turcotte, D. L., Guzzetti, F., and Reichenbach, P.: Landslide inventories and their statistical properties, *Earth*
554 *Surf. Process. Landf.*, 29, 687-711, <https://doi.org/10.1002/esp.1064>, 2004.

555 Matasci, B., Stock, G. M., Jaboyedoff, M., Carrea, D., Collins, B. D., Guerin, A., Matasci, G., and Raveland, L.: Assessing
556 rockfall susceptibility in steep and overhanging slopes using three-dimensional analysis of failure mechanisms, *Landslides*,
557 15, 859-878, <https://doi.org/10.1007/s10346-017-0911-y>, 2018.

558 Pérez-Rey, I., Muñiz-Menéndez, M., González, J., Vagnon, F., Walton, G., and Alejano, L. R.: Laboratory physical modelling
559 of block toppling instability by means of tilt tests, *Eng. Geol.*, 282, 105994, <https://doi.org/10.1016/j.enggeo.2021.105994>,
560 2021.

561 Pierson, L. A., Davis, S. A., and Van Vickle, R.: Rockfall hazard rating system—implementation manual, Federal Highway
562 Administration (FHWA), Report FHWA—OR-EG-90-01, FHWA, US Department of Transportation, 80 pp., 1990.

563 Sagaseta, C.: On the Modes of Instability of a Rigid Block on an Inclined Plane, *Rock Mech. Rock Eng.*, 19, 261-266,
564 <https://doi.org/10.1007/Bf01039998>, 1986.

565 Santi, P. M., Russell, C. P., Higgins, J. D., and Spriet, J. I.: Modification and statistical analysis of the Colorado Rockfall
566 Hazard Rating System, *Eng. Geol.*, 104, 55-65, <https://doi.org/10.1016/j.enggeo.2008.08.009>, 2009.

567 Tang, H. M., Wang, L. F., Chen, H. K., and Xian, X. F.: Collapse sequence of perilous rock on cliffs with soft foundation,
568 *Chinese Journal of Geotechnical Engineering*, 32, 205-210, 2010.

569 Volkwein, A., Schellenberg, K., Labiouse, V., Agliardi, F., Berger, F., Bourrier, F., Dorren, L. K. A., Gerber, W., and
570 Jaboyedoff, M.: Rockfall characterisation and structural protection – a review, *Nat. Hazards Earth Syst. Sci.*, 11, 2617-2651,
571 <https://doi.org/10.5194/nhess-11-2617-2011>, 2011.

572 Ward, D. J., Berlin, M. M., and Anderson, R. S.: Sediment dynamics below retreating cliffs, *Earth Surf. Process. Landf.*, 36,
573 1023-1043, <https://doi.org/10.1002/esp.2129>, 2011.

574 Wu, L. Z., Zhang, L. M., Zhou, Y., Xu, Q., Yu, B., Liu, G. G., and Bai, L. Y.: Theoretical analysis and model test for rainfall-
575 induced shallow landslides in the red-bed area of Sichuan, *Bull. Eng. Geol. Environ.*, 77, 1343-1353,
576 <https://doi.org/10.1007/s10064-017-1126-0>, 2018.

577 Yu, B., Ma, E., Cai, J., Xu, Q., Li, W., and Zheng, G.: A prediction model for rock planar slides with large displacement
578 triggered by heavy rainfall in the Red bed area, Southwest, China, *Landslides*, 18, 773-783, [https://doi.org/10.1007/s10346-
579 020-01528-x](https://doi.org/10.1007/s10346-020-01528-x), 2021.

580 Zhan, J., Yu, Z., Lv, Y., Peng, J., Song, S., and Yao, Z.: Rockfall Hazard Assessment in the Taihang Grand Canyon Scenic
581 Area Integrating Regional-Scale Identification of Potential Rockfall Sources, *Remote Sens.*, 14, 3021,
582 <https://doi.org/10.3390/rs14133021>, 2022.

583 Zhang, K., Tan, P., Ma, G. W., and Cao, P.: Modeling of the progressive failure of an overhang slope subject to differential
584 weathering in Three Gorges Reservoir, China, *Landslides*, 13, 1303-1313, <https://doi.org/10.1007/s10346-015-0672-4>, 2016.

585 Zhang, M., Yin, Y. P., and Huang, B. L.: Mechanisms of rainfall-induced landslides in gently inclined red beds in the eastern
586 Sichuan Basin, SW China, *Landslides*, 12, 973-983, <https://doi.org/10.1007/s10346-015-0611-4>, 2015.

587 Zheng, L. N., Chen, J. B., Zhou, Q. J., Feng, S. Q., Luo, Y. B., and Shen, P.: Experimental study on bearing capacity of
588 moderately weathered mudstone in Chengdu area, *Chinese Journal of Geotechnical Engineering*, 43, 926-932,
589 <https://doi.org/10.11779/CJGE202105017>, 2021.

590 Zhou, C., Yin, K. L., Cao, Y., Ahmed, B., Li, Y. Y., Catani, F., and Pourghasemi, H. R.: Landslide susceptibility modeling
591 applying machine learning methods: A case study from Longju in the Three Gorges Reservoir area, China, *Comput. Geosci.*,
592 112, 23-37, <https://doi.org/10.1016/j.cageo.2017.11.019>, 2018.

593 Zhou, Y., Shi, S., Zhang, Y., Cai, Q., Liang, J., and Cheng, Y.: Stability of unstable rock in nearly-horizontal sandstone-
594 mudstone stratum due to enlarged rock-cell, *Journal of Engineering Geology*, 25, 1220-1229,
595 <https://doi.org/10.13544/j.cnki.jeg.2017.05.006>, 2017.

596